Examining the Relationship between Cloud and Radiation Quantities Derived from Satellite Observations and Model Calculations

Fu-Lung Chang and Zhanqing Li

Canada Centre for Remote Sensing, Ottawa, Ontario, Canada

Steven A. Ackerman

Department of Atmospheric and Oceanic Sciences, University of Wisconsin—Madison, Madison, Wisconsin

ABSTRACT

This study examines the consistency and inconsistency in shortwave (SW) top-of-atmosphere (TOA) reflectances and albedos obtained from satellite measurements of the Earth Radiation Budget Experiment (ERBE) and radiation modeling based on cloud properties retrieved from the Advanced Very High Resolution Radiometer (AVHRR). The examination focuses on completely overcast scenes covered by low-level, single-layered, maritime stratus with uniform cloud-top heights as determined from AVHRR measurements at near nadir. A radiation model was then applied to the retrieved cloud optical depths, droplet effective radii, and top temperatures to compute the SW TOA reflectances and albedos that are compared with coincident ERBE observations. ERBE-observed and AVHRR-based modeled reflectances show excellent agreement in terms of both trend and magnitude, but the two albedos exhibit significant differences that have a strong dependence on cloud optical properties and solar zenith angle (SZA). To unravel the differences, two major factors, that is, scene identification and angular dependence model (ADM), involved in converting reflectance to albedo are examined. It is found that the dependence is mainly caused by the use of a single ERBE–ADM for all overcast scenes, regardless of cloud optical properties. The mean difference in SW TOA flux is about 4–12 W m^{-2}, depending on SZA, but individual differences may reach up to 40–50 W m^{-2} for persistent large or small cloud optical depths. Nearly all of the uniform low-level overcast scenes as determined by AVHRR are identified as mostly cloudy by ERBE, but the misidentification does not have any adverse effect on the albedo differences. In fact, replacing the ERBE mostly cloudy ADM with the overcast ADM exacerbates the albedo comparisons. The mean fluxes obtained with the two ADMs differ by ~8 W m^{-2} at SZA ≈ 33° and by 30 W m^{-2} at SZA ≈ 60°.

1. Introduction

To understand and model the earth's radiation budget (ERB) requires a good knowledge of cloud, radiation, and their interactions (Stephens et al. 1981; Hartmann et al. 1986; Arking 1991; Liou 1992). Much knowledge has been gained from both observations and modeling (Stephens and Platt 1987; Chou 1992; Lau and Crane 1995; Li et al. 1995; Rossow and Zhang 1995; Arking et al. 1996). The Earth Radiation Budget Experiment (ERBE; Barkstrom and Smith 1986) is one of the most successful spaceborne programs for studying the ERB, and it has been employed widely for climate studies. Applications include understanding the variations of ERB (Barkstrom et al. 1989; Harrison et al. 1990) and the role of clouds in altering the ERB (Ramanathan et al. 1989), and diagnostic studies of general circulation

models (Kiehl and Ramanathan 1990; Cess et al. 1992; Barker et al. 1994).

The Advanced Very High Resolution Radiometer (AVHRR) has long been the workhorse for retrieving cloud properties (Rossow and Schiffer 1991; Han et al. 1994; Platnick and Twomey 1994; Nakajima and Nakajima 1995; Platnick and Valero 1995; Han et al. 1999). Following the method proposed originally by Arking and Childs (1985), AVHRR channels centered nominally at 0.63, 3.7, and 11 μm have been successfully used to retrieve three key cloud variables, including optical depth, droplet effective radius, and top emission temperature.

In this study, the relations between both shortwave (SW) top-of-atmosphere (TOA) reflectance and albedo and cloud optical properties are explored by using coincident ERBE and AVHRR satellite observations. Such a study helps identify problems in both observations and modeling and allows examination of the fundamentals of radiative transfer process in clouds. By conventional radiative transfer theory, cloud reflectances

Corresponding author address: Dr. Zhanqing Li, Canada Centre for Remote Sensing, 588 Booth Street, Ottawa, ON K1A 0Y7 Canada. E-mail: li@ccrs.nrcan.gc.ca

are governed primarily by three variables, namely, extinction cross section, single-scattering albedo, and asymmetry factor. These variables have been parameterized to a good degree of accuracy by cloud liquid/ice water path and effective particle radius (e.g., Stephens 1978; Slingo 1989; Hu and Stamnes 1993; Fu 1996). However, due to some recent reports on large cloud absorption anomaly (Cess et al. 1995; Ramanathan et al. 1995; Pileskie and Valero 1995), the fundamentals of cloud radiative transfer need tests. More insight may be gained on the issue by examining the observed and modeled relationships between the TOA radiative quantities and cloud optical properties.

Examining the TOA albedo and its relation to cloud optical properties is also instrumental in assessing and improving the performance of satellite inversion algorithms. In dealing with satellite-derived flux/albedo datasets like those from ERBE, one must bear in mind that many inversion processes are involved (Smith et al. 1986). These inversion processes are potential sources of uncertainties, such as scene identification and angular correction (Stuhlmann and Raschke 1987; Baldwin and Coakley 1991; Li and Leighton 1991; Li 1996; Ye and Coakley 1996; Wielicki et al. 1996). An inadequate treatment in any of the inversion processes would lead to disagreement between observed and modeled relationships between TOA albedo and cloud optical properties. Thereby, a finding of any significant and systematic disagreements is helpful to unveil major deficiencies in the inversion processes. Likewise, flaws in the radiative transfer model may also be disclosed.

To avoid uncertainties incurred by nonhomogeneous clouds, the current study is concentrated on completely overcast scenes that were covered by uniform, low-level, single-layered, marine clouds in order to maximize the validity of the plane-parallel radiative transfer modeling. The following section describes the ERBE and AVHRR data used in this study. Section 3 explains the procedures of data analysis and radiative transfer modeling. The results are presented in section 4. Summary and discussions are given in the last section.

2. ERBE and AVHRR satellite data

The ERBE and AVHRR data used in this study were obtained from *NOAA-9* and *NOAA-10* polar-orbiting satellites, each of which carried both radiometers. The data were contained in the ERBE V-5 scene identification validation dataset. They were divided approximately into 10-min orbital segments over 20 geographically distinct locations of the earth, sampled every 5–6 days. Measurements taken over two V-5 regions from April and July 1985–88 were employed here. The two regions are located in the southeastern Pacific Ocean (5°–35°S, 80°–110°W) off the coast of South America and the central North Atlantic Ocean (15°–45°N, 30°–60°W). The months, locations, and satellites of data acquisition are listed in Table 1. Each V-5 segment covered an area

TABLE 1. Months, locations, and satellites.

	Southeastern Pacific (5°–35°S, 80°–110°W)	North Atlantic (15°–45°N, 30°–60°W)
NOAA-9	Apr 1985, Apr 1986, Jul 1985, Jul 1986	Jul 1985, Jul 1986
NOAA-10	Jul 1987, Jul 1988	Jul 1987, Jul 1988

of approximately 3400 km $\times$ 2400 km from limb to limb with maximum viewing zenith angle (VZA) $\approx 75°$, but only the data with VZAs less than 30° are analyzed here. These two regions were chosen because of the frequent occurrence of uniform, low-level, single-layered, marine status and stratocumulus clouds.

ERBE was designed to observe the broadband SW (0.2–5 μm) and longwave (5–50 μm) radiation budgets at the TOA with scanning and nonscanning radiometers. Only the data from the scanning radiometer, which has a higher spatial resolution, are used here. Also, this study focuses on the SW solar radiation. The spatial resolution of an ERBE scanner pixel at nadir field of view (FOV) is approximately 45 km for both the *NOAA-9* and *NOAA-10* satellites. The scanner measured instantaneous radiances from particular satellite viewing directions. The radiances were converted into TOA radiative fluxes using the scene-dependent ERBE SW angular dependence models (ADMs) (Smith et al. 1986). The ERBE scene identification was based on the maximum likelihood estimate (MLE) method as described in Wielicki and Green (1989). The ERBE ADMs were developed based primarily on the ERB data collected by the *Nimbus-7* for 12 scene types, including four categories of cloud amount and various surface conditions (Suttles et al. 1988). The ERBE ADMs had no dependence on cloud optical properties because a cloud imager like AVHRR was not available on the *Nimbus-7* satellite.

The AVHRR imager has a multispectral detector that measures radiances at five channels, namely, 0.63 (0.56–0.68), 0.89 (0.72–0.98), 3.7 (3.55–3.93), 11 (10.3–11.3), and 12 (11.5–12.5) μm. These channels are appropriate for studying the surface and cloud radiative properties because of weak gaseous absorption. An AVHRR pixel has a spatial resolution of approximately $(1.1 \text{ km})^2$ at nadir FOV. A spatially degraded AVHRR dataset, known as the global area coverage (GAC), was used for this study (Kidwell 1991). The GAC data have a reduced resolution of approximately 4 km at nadir. Three major cloud properties, including optical depth, droplet effective radius, and top temperature, were retrieved from AVHRR 0.63-, 3.7-, and 11-μm radiances using a cloud retrieval model developed by Chang (1997). The calibration and spectral response function of *NOAA-9* and *NOAA-10* were described in Kidwell (1991). Postlaunch calibration was also applied to AVHRR 0.63- and 11-μm radiance measurements, following the calibration method used in the International Satellite Cloud Cli-

matology Project (ISCCP, Brest et al. 1997). Other imaging radiometers like *NOAA-10* were all normalized to the *NOAA-9* standard to correct for any drift. The calibration also took advantage of a number of aircraft observation campaigns conducted during the lifetime of *NOAA-9*. The uncertainties in absolute value were reported to be 0.01–0.02 for reflectance at 0.63-μm, which lead to a bias of $\sim$10% in the retrieved cloud optical depths, and 1–2 K for brightness temperatures at 11 μm. As for the 3.7-μm channel, no postlaunch calibration was applied due to the lack of a reliable method for the time being. Han et al. (1994) estimated that the uncertainty in the prelaunch calibration at this channel is similar to that of the 11 μm for brightness temperatures > 270 K.

Because of the different pixel resolutions and scanning geometries, coincident ERBE and AVHRR data were collocated following Ackerman and Inoue (1994). Given the large overlap of ERBE pixels ($\sim$35% at nadir), AVHRR GAC pixels were sampled and collocated for every other ERBE pixel in both along- and cross-track directions. Although ERBE also has an along-track scanning mode, this study employed cross-track measurements only. To ensure the quality of the collocated data, linear least squares fits were applied to examine the correlation between ERBE SW and AVHRR 0.63-μm reflectance measurements for each month and location. The linear relationship between the SW and visible albedos is consistent with that established by Li and Trishchenko (1999) based on independent satellite measurements from the Scanner for Radiation Budget (ScaRaB). Data that deviate from the linear fit by two standard deviations were eliminated in this study.

3. Analysis procedures

a. Identification of uniform low-level overcast scenes

To identify uniform, low-level, single-layered overcast scenes, the spatial coherence method (Coakley and Bretherton 1982) was applied to AVHRR 11-μm radiances to examine the local spatial variation of the 11-μm radiance field. Figure 1a illustrates the 11-μm spatial coherence analysis for a geographical region of $\sim$(200 km)^2, which covers the FOVs of 4 $\times$ 4 ERBE pixels. The data were obtained on 14 April 1986 over the southeastern Pacific Ocean. Each point in the figure gives the local mean (*x* axis) and standard deviation (*y* axis) of the 11-μm brightness temperature for an array of 2 $\times$ 2 pixels. The arch distribution with two feet as seen in the figure is typical of a uniform, single-layered, marine stratus system (Coakley and Bretherton 1982). The foot near 291 K is emissions from the clear ocean background; another one near 282 K is from the top of a uniform, low-level cloud; and the body of the arch is composed of partly cloudy pixels. Shown in Fig. 1b are the AVHRR pixels that reside within a completely over-
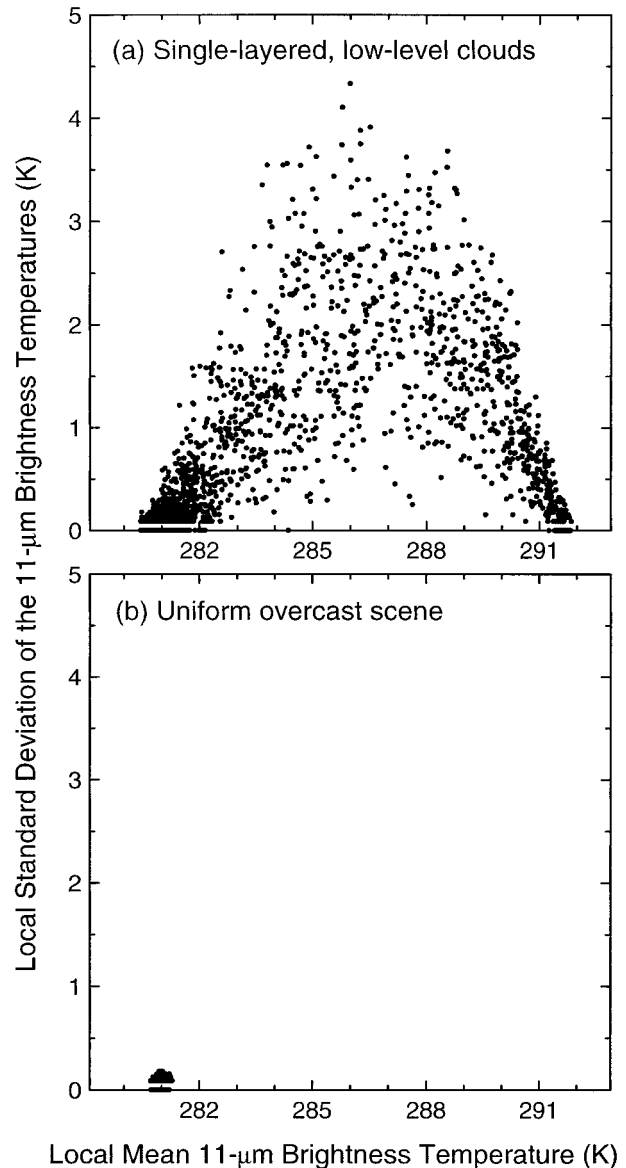
FIG. 1. Local mean 11-μm brightness temperatures and local standard deviations. Each point shows the mean and standard deviation for (a) a 2 $\times$ 2 array (8 km $\times$ 8 km) of the AVHRR GAC pixels taken from a geographical region of $\sim$(200 km)^2 and (b) a subregion of $\sim$(50 km)^2 extracted from (a).

cast FOV of an ERBE pixel covered by uniform, low-level, single-layered clouds. The selections of uniform and completely overcast scenes are based on the ERBE pixel scale, that is, all AVHRR pixels falling within an ERBE pixel are completely overcast. The narrow range of the 11-μm brightness temperature in Fig. 1b indicates that the cloud-top heights were rather uniform. To ensure the uniformity, the standard deviation of all AVHRR 11-μm brightness temperatures within a completely overcast ERBE pixel has to be less than 1 K and the selected uniform overcast ERBE pixel must be surrounded by overcast pixels.
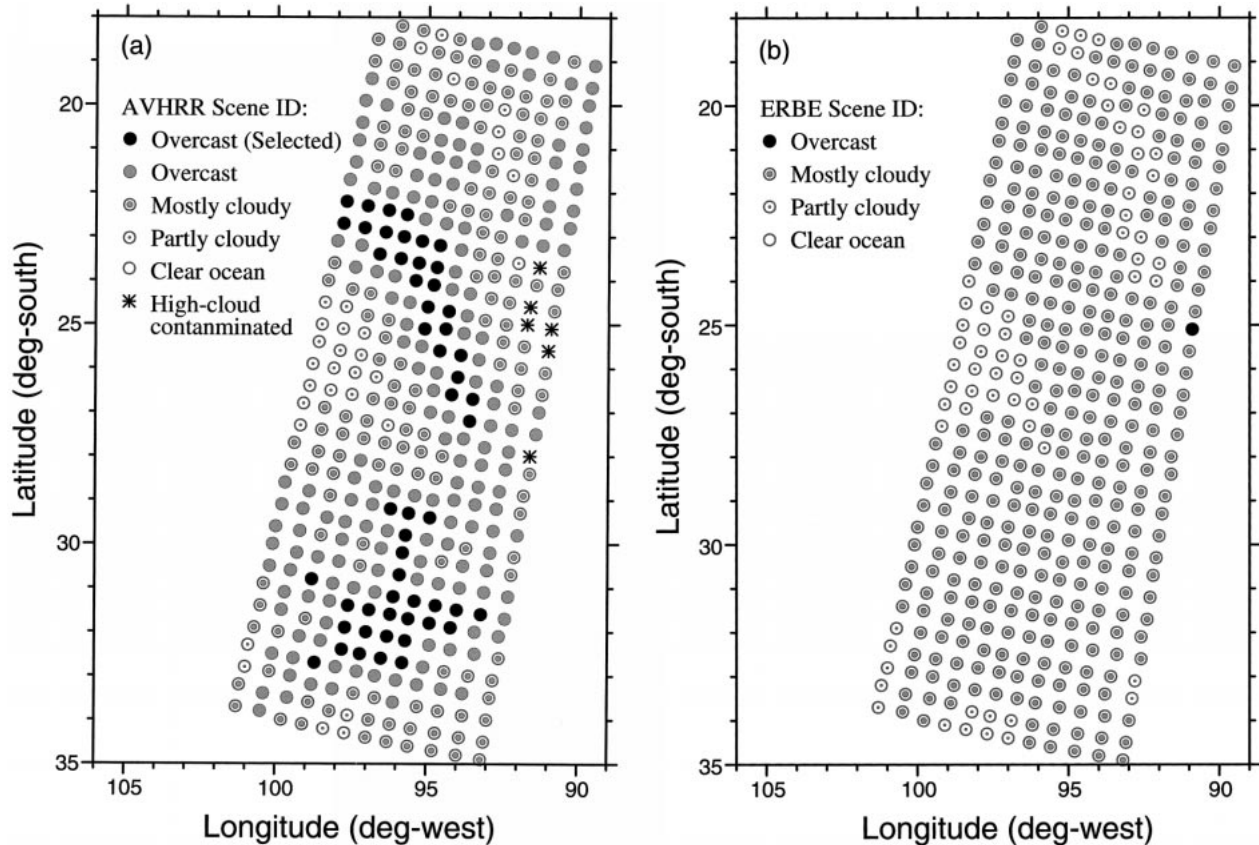
FIG. 2. Scene identifications based on the (a) AVHRR and (b) ERBE data. The results were obtained from a 10-min orbital pass with satellite VZAs $< 30°$. Each symbol represents the FOV of an ERBE pixel, $\sim(50$ km$)^2$ geographically. The selected overcast scenes denoted in (a) are completely covered with uniform, low-level, single-layered clouds.

Because a uniform radiance field may come from either a cloud layer with flat-top height or a clear ocean surface, statistical analyses were made over a large region $>(200$ km$)^2$ to distinguish the two (Coakley and Baldwin 1984). Besides, the mean cloud-top emission temperatures were restricted to higher than 273 K to ensure that the selected low-level clouds are only composed of water droplets. Figure 2 compares the scene identification for the ERBE-pixel scale based on (Fig. 2a) the spatial coherence analysis applied to AVHRR data and (Fig. 2b) the ERBE MLE method. The figure shows observations for a 10-min orbital segment that was obtained on 14 April 1985 near the coast of Chile, where a low-level marine stratus meanders in the region. The selected overcast scenes as shown in Fig. 2a are identified as being completely covered by low-level, single-layered system with uniform cloud-top heights according to AVHRR scene identification. However, only one of the ERBE pixels in the entire region was identified as being overcast by the ERBE MLE method. The majority of the remaining pixels were identified by ERBE as being mostly cloudy and a small fraction as partly cloudy. The ERBE overcast scenes generally correspond to relatively cold clouds with temperatures be-

low 270 K. Because of such large discrepancies in scene identification, this study applied the ERBE ADMs for both overcast and mostly cloudy scene types to the AVHRR-based overcast scenes to examine the differences in the angular conversion of reflectance to albedo.

b. Retrieval of cloud optical properties

An iterative scheme was used to retrieve cloud optical depths, droplet effective radii, and top temperatures from AVHRR radiance measurements at 0.63, 3.7, and 11 μm (Chang 1997). The retrieval scheme is similar to those of Han et al. (1994) and Nakajima and Nakajima (1995). It compares AVHRR radiance measurements to lookup tables of simulated radiance from radiative transfer model calculations for the corresponding sun–earth–satellite viewing geometry. Cloud optical depth, top temperature, and droplet effective radius are retrieved in an iterative manner from AVHRR measurements at the 0.63-, 11-, 3.7-μm channels, respectively. During the iteration process, a cloud property newly retrieved at one channel was updated for retrieving next cloud property with another channel. The iteration process ter-
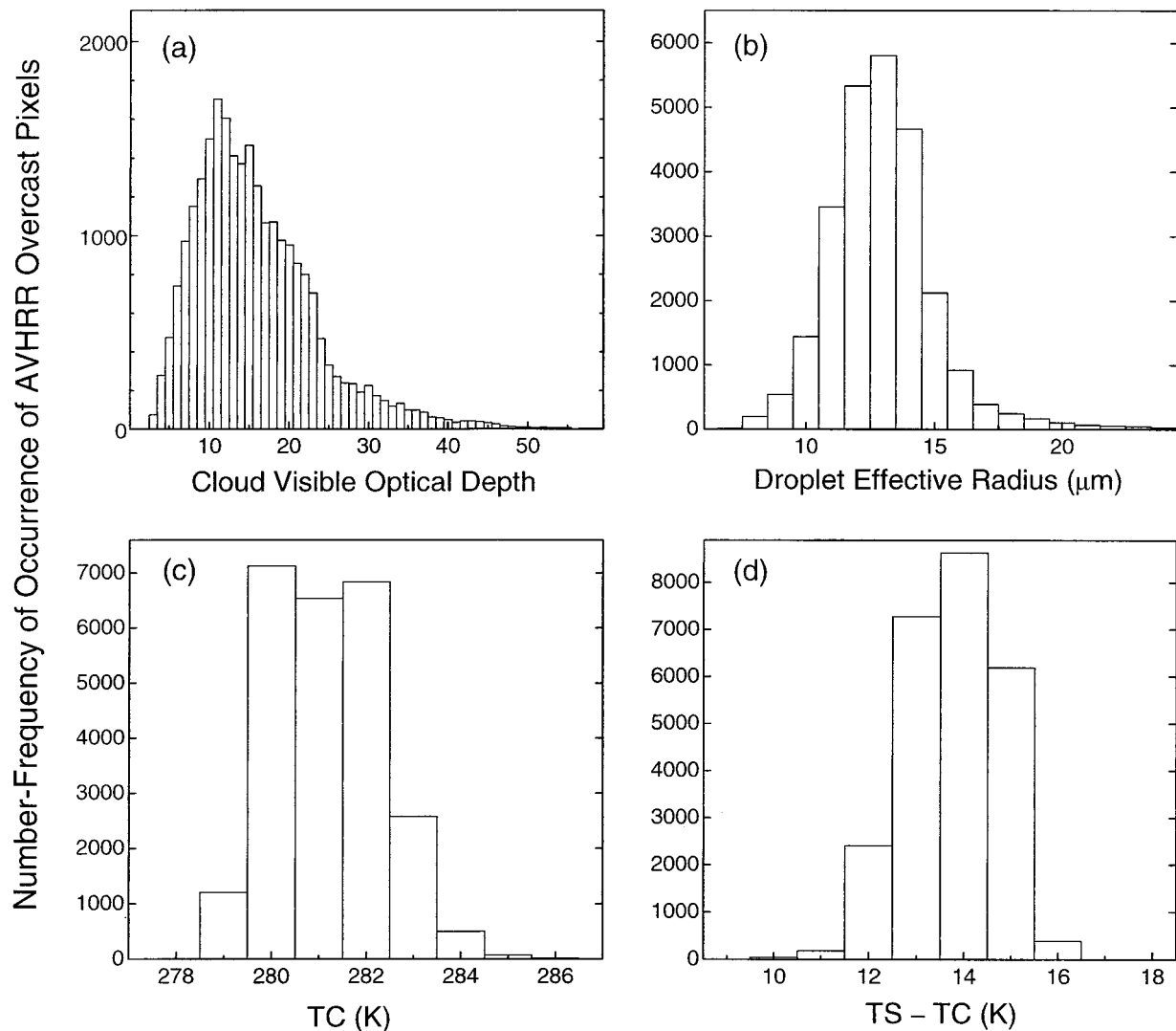
FIG. 3. Number frequency of occurrence of the (a) cloud visible optical depth, (b) droplet effective radius, (c) cloud-top temperature (TC) and (d) the difference between surface temperature (TS) and TC. The numbers are for the AVHRR pixels collocated within the selected uniform overcast scenes, as shown in Fig. 2a.

minates when all retrieved cloud properties converge to stable values.

Figure 3 shows the frequency distributions (number of occurrence) of cloud visible optical depth, droplet effective radius, cloud-top temperature (TC), and the difference between the clear ocean brightness temperature (TS) and TC for the uniform overcast scenes selected in Fig. 2a. It is seen that the low-level, single-layered cloud system in the region has a rather uniform TC, which is generally about 280–282 K (Fig. 3c). The difference (TS − TC) is about 12–15 K (Fig. 3d), typical of marine boundary layer clouds (Betts et al. 1992). The cloud visible optical depths range from 5 to 40 (Fig. 3a) and droplet effective radii from 10 to 16 μm (Fig. 3b), similar to previous findings (Nakajima et al. 1991; Han et al. 1994; Platnick and Valero 1995; Nakajima and Nakajima 1995).

c. Model computation of SW reflectance and albedo

For each overcast ERBE pixel, both SW TOA reflectance and albedo were calculated based on the AVHRR-retrieved cloud properties using an adding–doubling radiative transfer model (e.g., Goody and Yung 1989). The SW broadband calculations were made at 110 spectral bands of varying bandwidths spanning from 0.2 to 5 μm. For comparison with ERBE data, model calculations were first conducted at AVHRR pixel scale and then the calculated SW reflectances and albedos were averaged over the FOV of an ERBE pixel.

The reflectances were calculated at 32 Gauss quadrature points in the zenith direction (16 upward and 16 downward), 19 angles (0°, 10°, . . . , 180°) in the azimuth direction, 20 cloud visible optical depths (0.1, 1, . . . , 256), and 15 droplet effective radii (3, 4, . . . , 32 μm). The Mie

theory (Bohren and Huffman 1983) was used to calculate the scattering and absorption properties of water droplets. A gamma size distribution with an effective variance of 0.13 was assumed (Hansen 1971). The complex refractive index of water was taken from Hale and Querry (1973). The LOWTRAN7 (Kneizys et al. 1988) and standard mid-latitude atmospheric models (McClatchey et al. 1972) were adopted to correct for the atmospheric molecular scattering and absorption. A maritime aerosol model included in the LOWTRAN7 was used with a total optical depth of 0.1 distributed between 0 and 4 km. The extraterrestrial solar spectral radiances were taken from Thekaekara (1974). A Lambertian reflectance of 0.06 for the entire solar spectrum was assumed for the ocean surface (Payne 1972). Cloud layer was assumed to be 1 km in vertical thickness with a relative humidity of 100%. The cloud-top height was estimated based on TS minus TC, using a lapse rate of 9.8 K km^{-1} (Rodgers and Yau 1989). The uncertainties of the model calculations were estimated by the changes in the model-input variables, including a factor of ± 2 in the column amount of atmospheric water vapor and ozone, 0–0.1 in surface albedo, 0–0.25 in aerosol optical depth, and ± 1 km in cloud-top height.

4. Results

a. Comparison of SW TOA reflectance

The SW overcast reflectances derived from model computations based on the cloud properties retrieved from AVHRR measurements (i.e., AVHRR modeled) are compared to ERBE observations for all overcast ERBE pixels identified based on the spatial coherence method. Figure 4 compares the ERBE-observed (open circle) and AVHRR-modeled (solid square) relationships between SW overcast reflectance and cloud optical depth. The comparisons are shown in five panels for different solar zenith angles (SZAs) that are associated with different months, regions, and imagers, as indicated in the figure. The SZAs given in the figure are the mean values, with the associated standard deviations generally around 3° given in parentheses. The bars indicate the potential ranges of uncertainties in the model computations due to variations in atmosphere and surface conditions as described earlier. It is seen that the ERBE-observed and AVHRR-modeled relationships between SW overcast reflectance and cloud optical depth are in good conformity with each other, in terms of both magnitude and trend of the variations. Moreover, such conformity has no dependence on either SZA or cloud optical depth. The mean differences between ERBE-observed and AVHRR-modeled SW reflectances are within 0.7%, as indicated in each panel, which is comparable to 0.6% of the calibration uncertainty for the instantaneous ERBE SW reflectance measurements (Wielicki et al. 1995). The root-mean-square (rms) differences between the observations and modeling are generally less than 1.8%, which is about the magnitude of uncertainty in AVHRR visible calibra-

tion and half the magnitude of the uncertainty in model calculations.

The results shown in Fig. 4 reveal that first the radiative transfer model employed here performs reasonably well in converting the spectral narrowband measurements from AVHRR to the broadband measurements from the ERBE over the entire solar spectrum. Regardless of the different SZAs, regions, and months, there is no systematic bias in the conversion process, at least for the nadir-view, low-level, single-layered, marine overcast systems as analyzed here. Second, the absolute calibrations of the *NOAA-9* and *NOAA-10* AVHRR data are consistent with the calibrations of the ERBE measurements. ERBE had an onboard absolute calibration system (Barkstrom and Smith 1986), whereas the ISCCP calibration for the AVHRR data was made indirectly after launch. The calibration of AVHRR data was based on the assumption that the reflectivity of the whole globe remains constant, which can be traced to measurements over some stable vicarious targets (Brest et al. 1997). The consistency in the two datasets is essential for studying the relationship between cloud and radiation quantities derived from both satellites. Of course, the possibility that there could be errors in both the radiative transfer modeling and calibration, which happen to cancel out each other, cannot be ruled out. If there is no error cancellation and if the calibrations are correct, the finding testifies that there are no fundamental problems concerning the radiative transfer in plane-parallel clouds (Li et al. 1995).

Figure 5 shows the differences between the ERBE-observed and AVHR-modeled SW overcast reflectances as a function of the following parameters: cloud visible optical depth, droplet effective radius, TC, and SZA. The left column shows results obtained from *NOAA-9* and the right column those from *NOAA-10*. Although the differences for *NOAA-10* show larger scattering than for *NOAA-9,* their mean differences are close and generally small. There is no significant dependence on any of the parameters from either *NOAA-9* or *NOAA-10,* implying that the retrievals and treatments in the radiation model are sound. In comparing the two satellites, ERBE observations are on average 0%–1% larger than the AVHRR-modeled values for *NOAA-9* but 0%–1.5% smaller for *NOAA-10*. The discrepancies may be attributed in part to the calibration biases between *NOAA-9* and *NOAA-10* in both ERBE and AVHRR measurements, and in part to the model uncertainties due to different overcast conditions for *NOAA-9* and *NOAA-10*. The latter are revealed in the figure, as cloud optical depths are larger for *NOAA-10* than for *NOAA-9* in terms of the mean and range and TCs on average are 2 K warmer for *NOAA-10* than for *NOAA-9,* indicating some differences in cloud-top height. The mean droplet effective radii are relatively close (11.9–11.6 μm).

b. Comparison of SW TOA albedos

Similar to Fig. 4, Fig. 6 shows the comparison of the relationships between SW TOA albedo and cloud op-
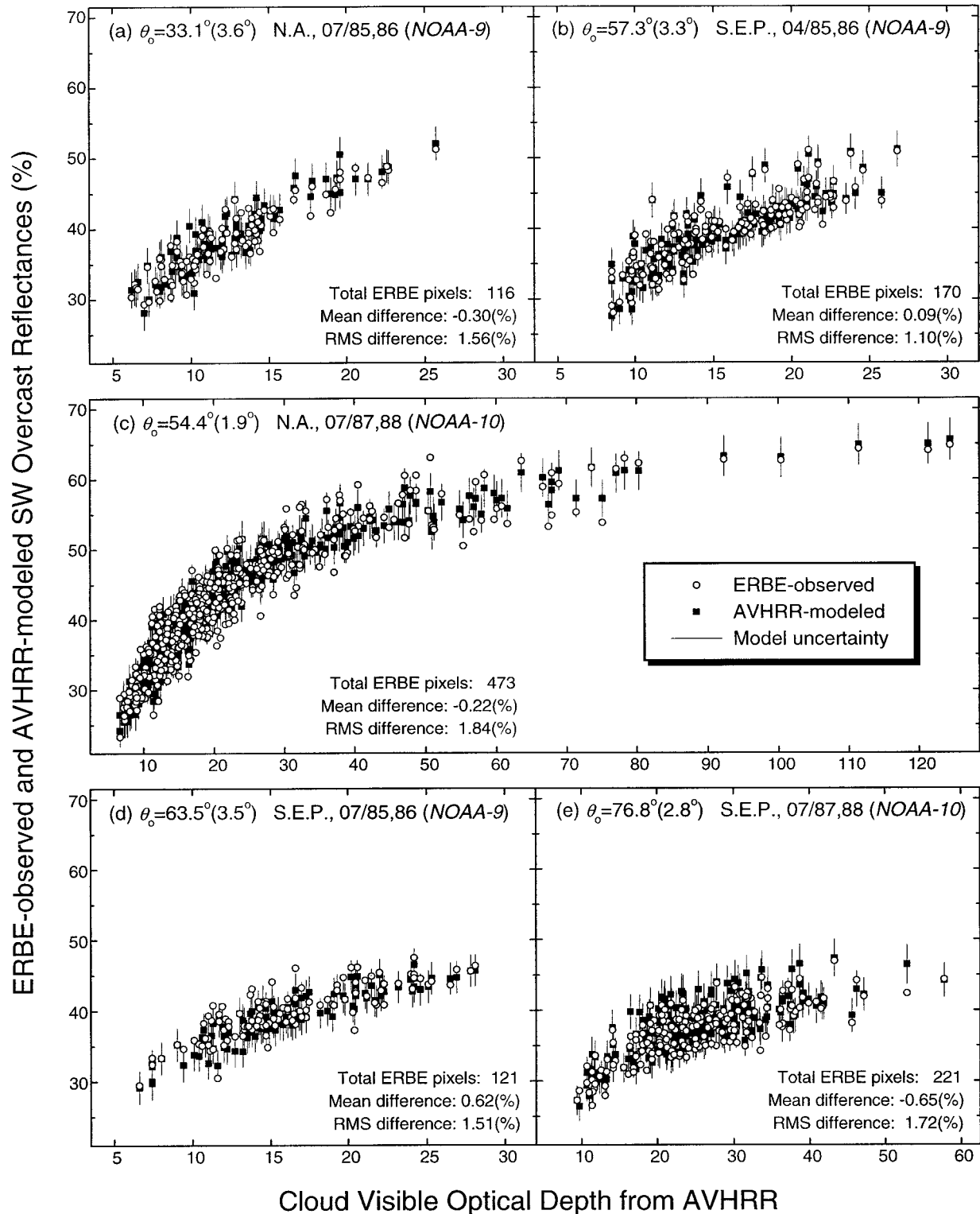
FIG. 4. Comparison of ERBE-observed and AVHRR-modeled SW overcast reflectances as a function of cloud visible optical depth. Each point is for a (50 km)^2 ERBE pixel. The cloud visible optical depth is an average for all AVHRR overcast pixels within the (50 km)^2 area. The bars denote the maximum ranges of uncertainties in the model calculations. The mean and rms differences between observed and modeled reflectances are indicated in each panel, along with regions, months, satellites, and SZAs of the observations.
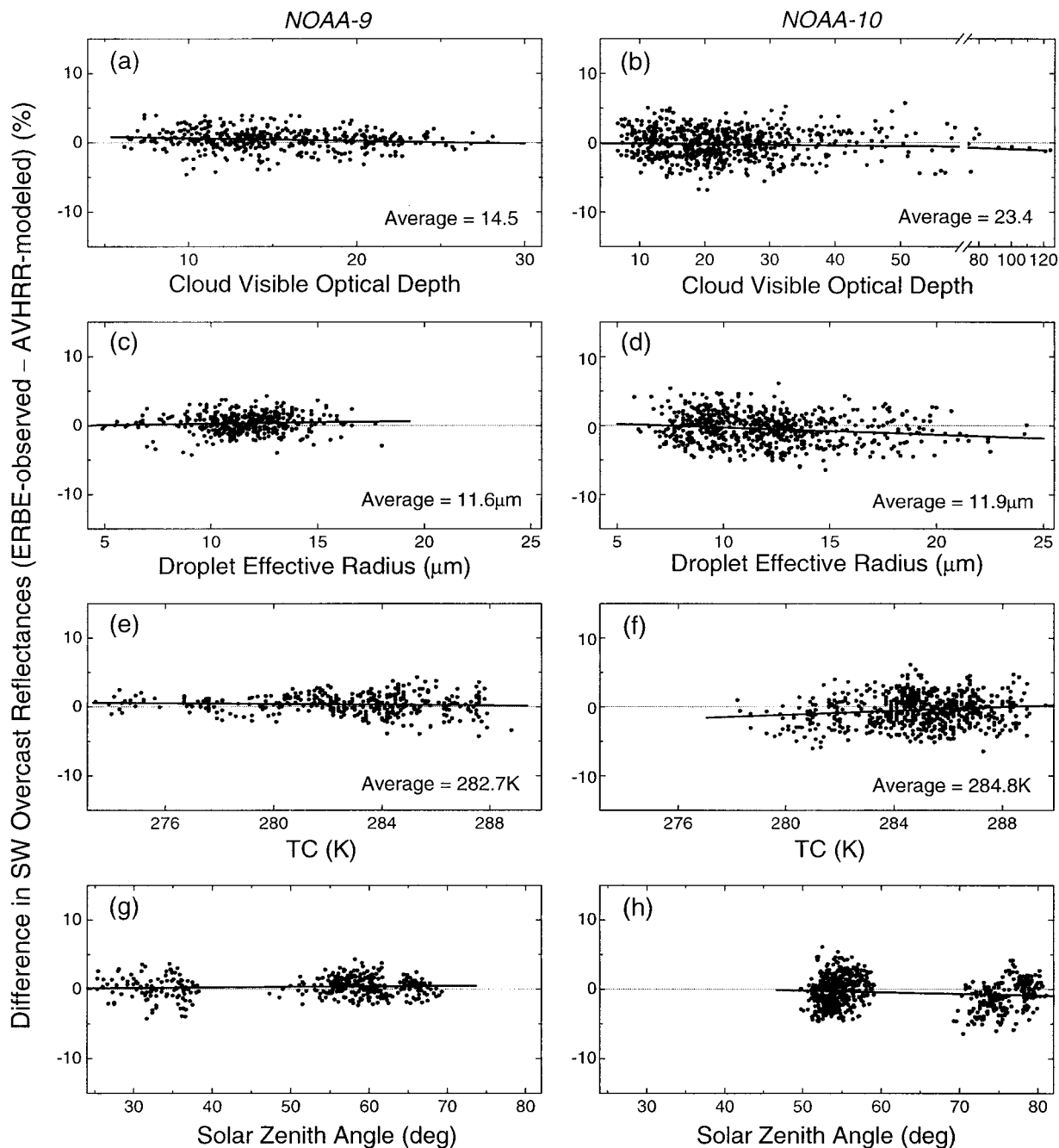
FIG. 5. Difference between ERBE-observed and AVHRR-modeled SW overcast reflectances as a function of [(a) and (b)] cloud visible optical depth, [(c) and (d)] droplet effective radius, [(e) and (f)] TC and [(g) and (h)] SZA. The left column shows results obtained from *NOAA-9* and the right column those from *NOAA-10*. The averages indicated in the figure are for cloud visible optical depth, droplet effective radius, and TC. Straight lines are the linear least squares fits.

tical depth. The figure compares the ERBE inverted albedos (open circles) to AVHRR-based modeled albedos (solid squares) as a function of cloud optical depth for all overcast ERBE pixels. Unlike the good agreements found in the reflectance comparisons, the albedos from ERBE and model computation display large discrepancies. In many cases, the differences between the two

albedos are beyond the maximum range of uncertainties in model computation. The mean difference between the two albedos is relatively small (0.0033) for SZA $\approx 33.1°$ but increases with increasing SZA to more than 0.03 (absolute value) for SZA $\approx 76.8°$. The magnitude of the uncertainty in regional monthly mean albedos as reported by Wielicki et al. (1995) is about 0.016, similar
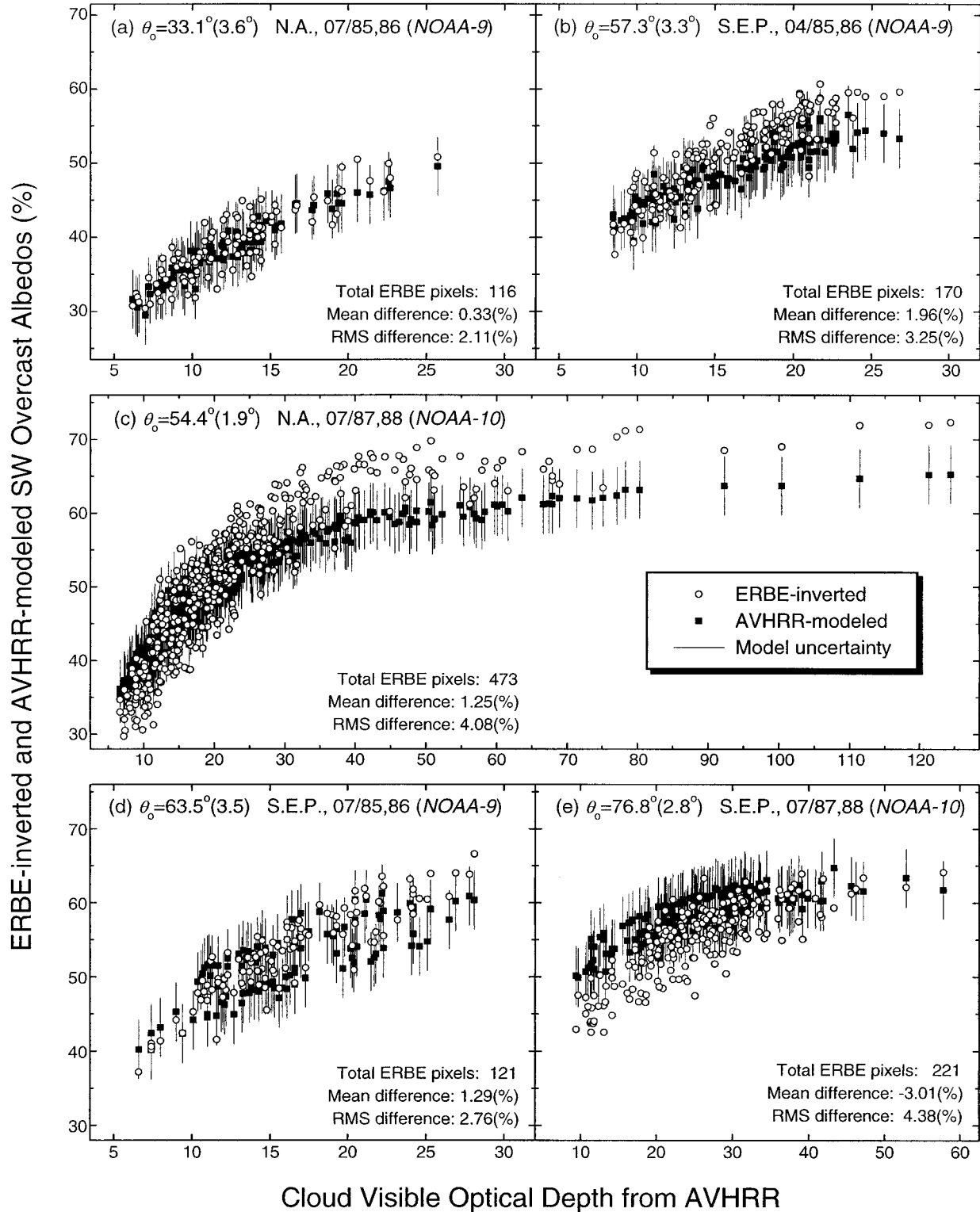
FIG. 6. Same as Fig. 4, but for the comparison of ERBE-inverted and AVHRR-modeled SW overcast albedos.
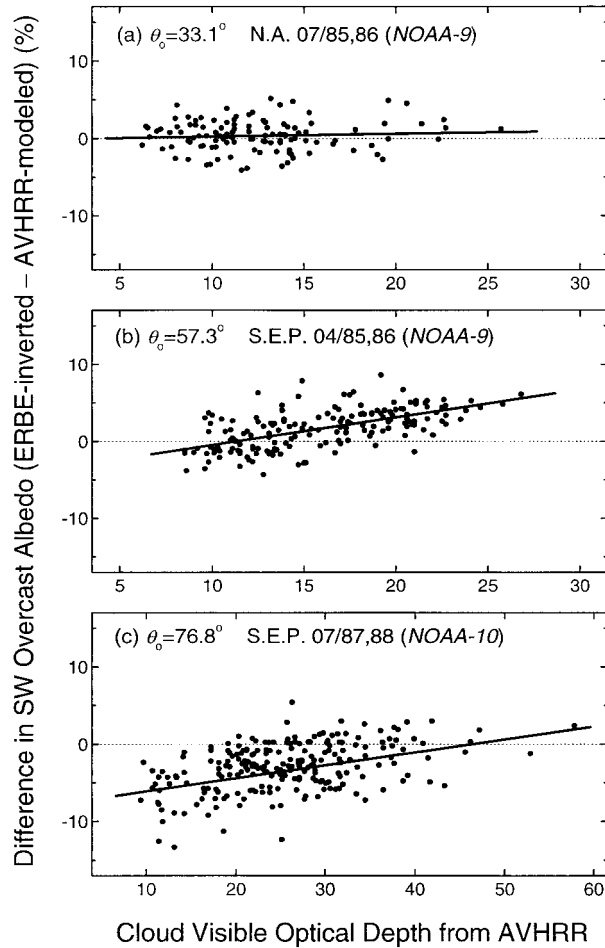
FIG. 7. Difference between ERBE-inverted and AVHRR-modeled SW overcast albedos as a function of cloud visible optical depth. Results are shown for three SZAs of (a) 33.1°, (b) 57.3°, and (c) 76.8°, as in Figs. 6a, 6b, and 6e. Straight lines are linear least squares fits.

to the mean differences obtained here for SZA around 60° (Figs. 6b–d). The rms differences between the two albedos are also indicated in the figure, ranging from about 0.021 to 0.044, which are comparable to the claimed uncertainty of about 0.038 for the instantaneous ERBE-inverted albedo due to both calibration and angular sampling (Wielicki et al. 1995).

In addition to the mean and rms differences, another feature revealed in Fig. 6 is that the difference has a strong dependence on cloud optical depth. The ERBE albedos increase more rapidly than the modeled ones with increasing cloud optical depth and attain larger values for large cloud optical depth. The dependence also varies with SZA. Figure 7 shows the albedo differences as a function of cloud optical depth for three SZAs. For SZA $\approx$ 33.1°, the mean difference is about zero with no obvious dependence on cloud optical depth. For SZA $\approx$ 57.3°, the overall mean difference is still small, but individual differences vary systematically

with cloud optical depth. ERBE albedos tend to be lower than modeled values for small cloud optical depth ($<$10) but higher for large cloud optical depth ($>$15). For SZA near 76.8°, ERBE albedos are generally lower than modeled ones and their differences seem to decrease with increasing cloud optical depth up to 50.

Given that good agreements exist between ERBE-observed and AVHRR-modeled reflectances, the discrepancies found for albedos must originate either from the conversion of ERBE-observed reflectance to albedo, or from the radiation modeling with regard to the integration of reflectance values to albedos, or from both.

ERBE albedos were inverted from reflectance measurements based on the ERBE ADM (Suttles et al. 1988). ERBE ADM, $R(\theta_0, \theta, \phi - \phi_0)$, defines the empirical relationship between mean TOA reflectance, $\overline{a}(\theta_0, \theta, \phi - \phi_0)$, and mean TOA albedo, $\overline{A}(\theta_0)$, for specific angular bins in the sun–earth–satellite viewing geometry. An ERBE ADM is given by

$$R(\theta_0, \theta, \phi - \phi_0) = \frac{\overline{a}(\theta_0, \theta, \phi - \phi_0)}{\overline{A}(\theta_0)}, \qquad (1)$$

where θ_0 denotes the SZA, θ the VZA, and $\phi_0 - \phi$ the relative azimuth angle (RAA) between the sun and satellite. The ERBE ADMs were developed for 12 scene types with respect to four different cloud amounts and four different background surfaces (Suttles et al. 1988). The cloud amount identified by ERBE determines which ADM is to be used for inverting reflectance to albedo. There is only one ADM for all overcast cloud scenes, regardless of cloud optical and microphysical properties. For an overcast scene, ERBE albedo, $\hat{A}(\theta_0)$, is then estimated by

$$\hat{A}(\theta_0) = \frac{a(C; \theta_0, \theta, \phi - \phi_0)}{R(\theta_0, \theta, \phi - \phi_0)}, \qquad (2)$$

where $a(C; \theta_0, \theta, \phi - \phi_0)$ is the measured reflectance that depends on the cloud optical and microphysical properties, denoted by C. As the ERBE overcast ADM, $R(\theta_0, \theta, \phi - \phi_0)$, has no dependence on C, the estimated ERBE albedos, $\hat{A}(\theta_0)$, must contain certain bias errors with regard to varying cloud optical and microphysical properties (Wielicki et al. 1996; Chang et al. 2000).

In the model calculations, an overcast albedo, $A'(C; \theta_0)$, was calculated from the following angular integration:

$$A'(C; \theta_0) = \frac{1}{\pi} \int_0^{2\pi} \int_0^{\pi/2} a'(C; \theta_0, \theta, \phi - \phi_0)$$
$$\times \cos\theta \, \sin\theta \, d\theta \, d\phi, \qquad (3)$$

where $a'(C; \theta_0, \theta, \phi - \phi_0)$ denotes the overcast reflectance that has a dependence on cloud optical and microphysical properties. Note that the cloud optical depth, droplet effective radius, and top temperature as inputs to the model calculations were retrieved from the

AVHRR measurements at near-nadir VZAs. The reflectances, $a'(C; \theta_0, \theta, \phi - \phi_0)$, at large VZAs calculated based on the cloud properties that retrieved at near nadir may suffer from angular bias due to the plane-parallel assumption in the radiation model (Loeb and Coakley 1998). This angular bias increases with increasing SZA, as the largest mean difference of about -0.03 occurs at SZA $\approx 76.8°$ (Fig. 6e).

Scene identification is another major factor dictating the ERBE reflectance-to-albedo conversion, as it determines which ADM to use. As stated earlier, nearly all of the uniform overcast scenes under study were assigned as mostly cloudy by ERBE (cf. Fig. 2). Consequently, the ERBE albedos for these overcast scenes were mainly converted based on the ERBE mostly cloudy ADM. One might think that such scene misidentification is responsible for, or at least contributes to, the discrepancies between ERBE and modeled albedos. To clarify this, ERBE albedos were modified by applying the ERBE overcast ADM in lieu of the mostly cloudy ADM to the ERBE reflectance measurements.

Figure 8 shows the same comparison as in Fig. 6, except using the ERBE overcast ADM. It is seen that the modified ERBE albedos are systematically smaller than the original ERBE albedos. However, there is no overall improvement in the comparison between ERBE-modified and AVHRR-modeled albedos. The mean differences between ERBE-modified and modeled albedos are generally larger in magnitude than the mean differences between original ERBE and modeled albedos. Note that the signs of the two mean differences have changed as well. Although some improvement can be found over certain ranges of cloud optical depths and SZAs, the comparisons at larger SZAs deteriorate considerably. For example, the modified ERBE albedos for SZA $\approx 76.8°$ (Fig. 8e) are overall much smaller than the AVHRR-modeled albedos with an rms difference of ~ 0.094. The magnitude of the mean difference increased almost three times from 0.03 (Fig. 6e) to 0.088 (Fig. 8e).

The finding here reveals that in applying an empirical ADM for angular conversion, like the ERBE ADM, one must use a scene identification method that is consistent with the scene identification method used in developing the ADM. Uses of inconsistent scene identification methods between the development and application of ADM, even if the latter method, as in the case of AVHRR, is more sound, can lead to significant errors in the angular conversion of reflectance/radiance to albedo/flux.

c. Comparisons of SW ADMs and TOA fluxes

To unravel the discrepancies between ERBE and modeled albedos, it is necessary to understand the differences between ERBE empirical ADMs and radiation-model simulated ADMs. Figure 9 shows the comparisons of the ERBE ADMs for both overcast and mostly

cloudy oceans to the model-simulated ADMs for overcast scenes with three different cloud optical depths (1, 16, and 256). The ERBE and modeled ADMs are depicted as a function of VZA in six panels for three SZAs (33°, 60°, and 77°) and two RAAs. The comparisons only show for near-nadir VZAs ($<35°$) because of the large uncertainties at large VZAs suffered by both the ERBE ADM (Suttles et al. 1992) and radiation model (Loeb and Coakley 1998). In the model simulations, a droplet effective radius of 10 μm, a maritime aerosol optical depth of 0.1, a standard midlatitude summer atmospheric model, and a Lambertain surface reflectance of 0.06 were used. The top three panels are for RAA $= 0°$, that is, the principle scattering plane; the bottom three panels are for RAA $= 50°$, a slantwise scattering plane.

For SZA $= 33°$ (Figs. 9a and 9d), the ERBE ADMs for overcast and mostly cloudy scenes are very close to each other with values near unity. They are also close to the modeled ADM for a cloud optical depth of 16. This infers that the ERBE albedos obtained using either the overcast or mostly cloudy ADM should be close and agree well with the modeled albedo for cloud optical depths near 16, which is the case in the comparisons shown in Figs. 6a (ERBE mostly cloudy ADM) and 8a (ERBE overcast ADM). Figures 9a and 9d also reveal that ERBE albedos are larger than the modeled values for larger cloud optical depths (cf. $\tau = 128$) and the opposite for smaller cloud optical depths (cf. $\tau = 1$). These are again consistent with the comparison results shown in Fig. 6.

For SZA $= 60°$ (Figs. 9b and 9e), ERBE overcast and mostly cloudy ADMs are significantly different from each other. The mostly cloudy ADM is still close to the modeled ADM for a cloud optical depth of 16, but the overcast ADM is close to the modeled ADM for a cloud optical depth near 40 (not plotted). This finding is reflected in the comparisons between Figs. 6b–d and 8b–d. For example, the ERBE-inverted albedos in Fig. 6c are close to the models at cloud optical depth around 16, but ERBE-modified ones in Fig. 8c are close at cloud optical depth near 40. As for SZA $= 77°$ (Figs. 9c and 9f), ERBE ADMs for both overcast and mostly cloudy scenes agree better with the modeled ADMs for larger optical depths than for smaller one. This is again consistent with the trends found in Figs. 6e and 8e, where the agreement improves significantly as cloud optical depth increases, although the systematic differences may stem, at least partially, from model uncertainties for large VZAs, as discussed earlier.

These analyses imply that the large discrepancies in albedo are mainly caused by the discrepancies in the ADMs, which vary with cloud optical depth and SZA. Since both cloud optical depth and SZA change with season and region on a global scale (Tselioudis et al. 1992), radiative fluxes obtained from ERBE may be subject to regional biases. Unfortunately, it is hard to quantify such regional biases, because the results pre-
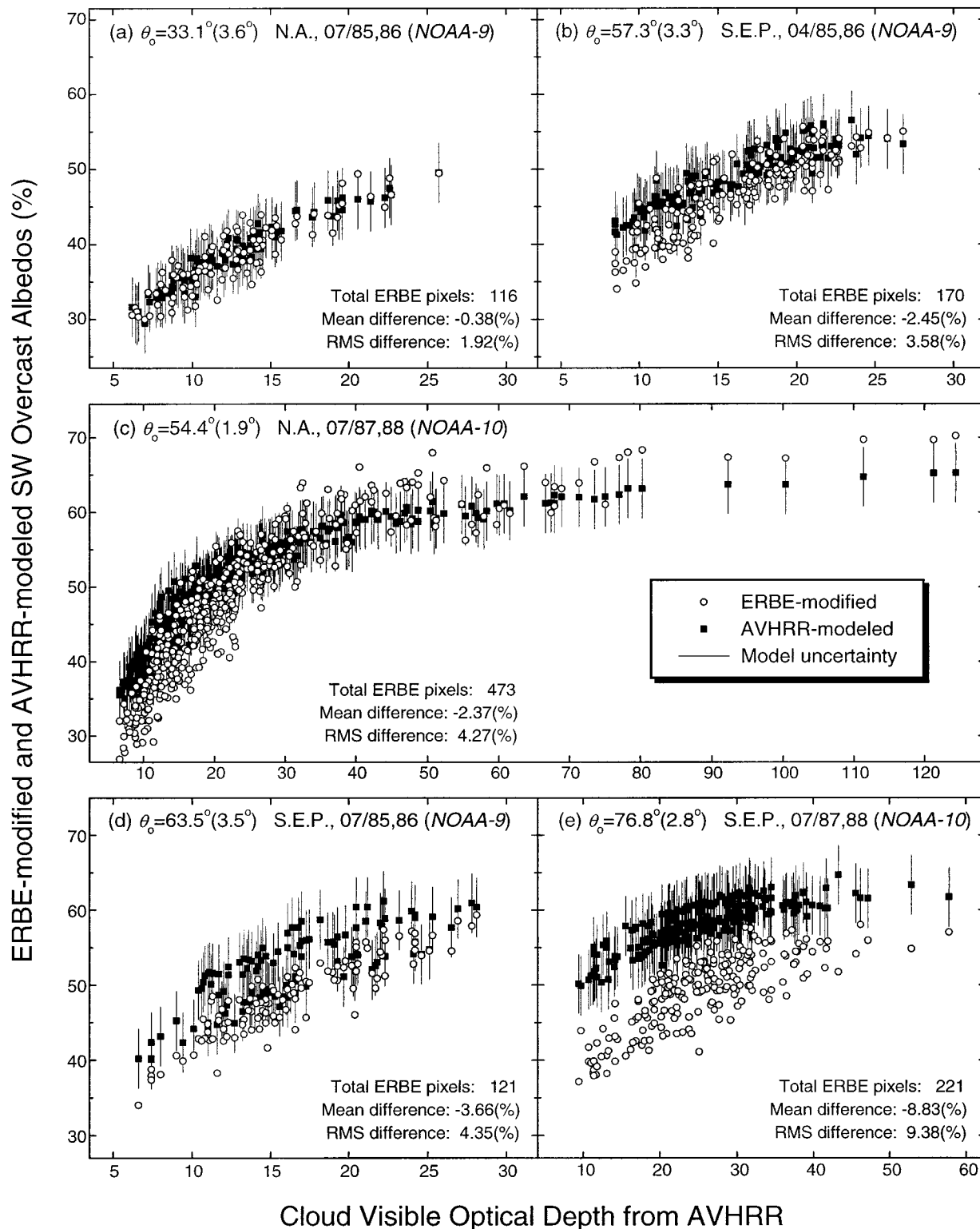
FIG. 8. Same as Fig. 6, but for the comparison of ERBE-modified and AVHRR-modeled SW overcast albedos.
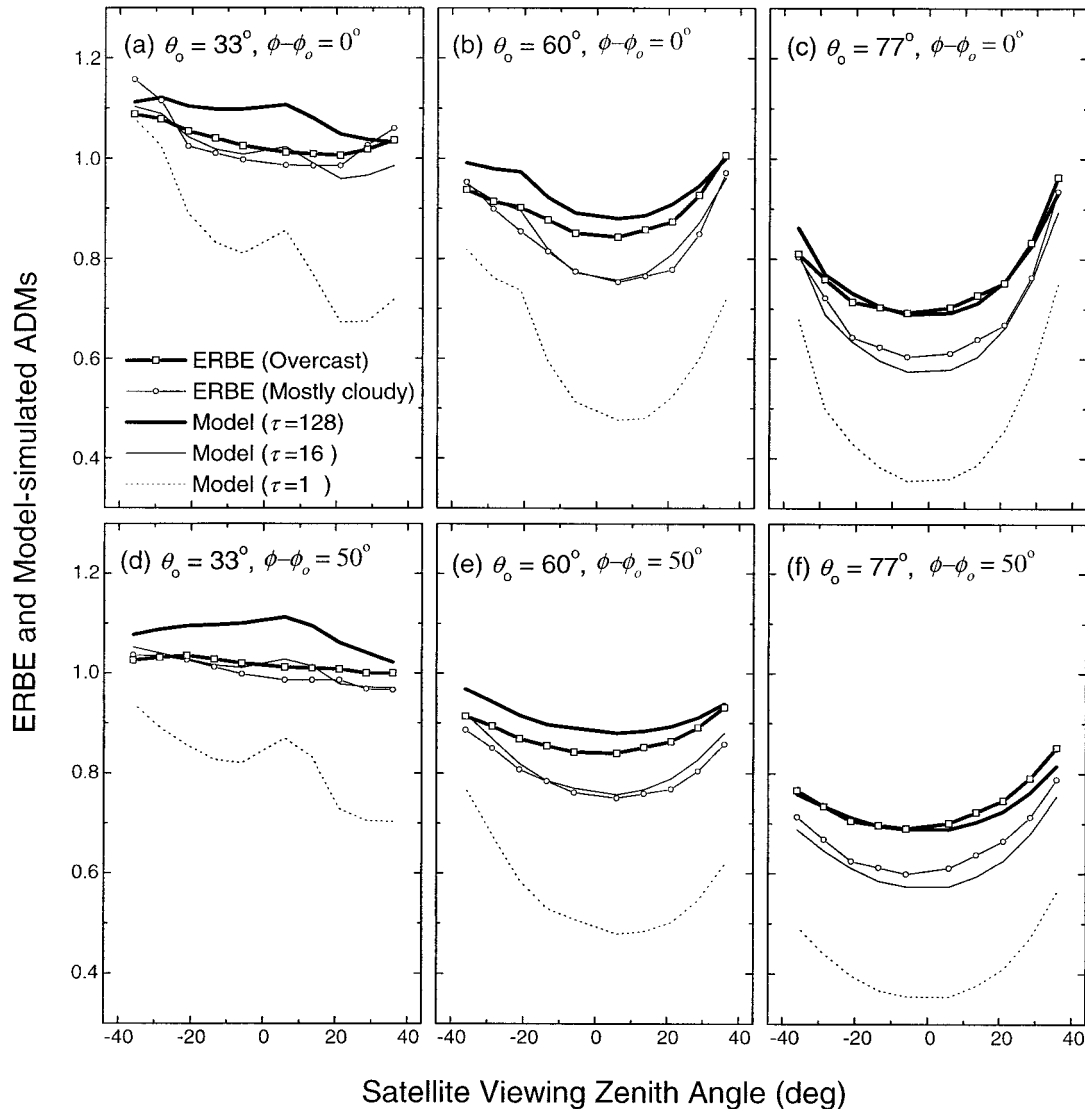
FIG. 9. Comparison of model-simulated and ERBE overcast and mostly cloudy ocean SW ADMs as a function of VZA. The ADMs are shown for two relative azimuth planes, (top) i.e., RAA = 0° and (bottom) 50°. Negative VZAs denote the backscattering (i.e., 180° − RAA) on the same azimuth plane. Three modeled ADMs are simulated for overcast scene with a cloud visible optical depth of 1, 16, and 128, based on the radiation model described in the text.

sented here are only valid for uniform clouds of relatively flat tops. In reality, all types of clouds may occur in each region causing errors of different magnitudes and even opposite signs. Nonetheless, one may gain an idea from Fig. 10 of the magnitude of potential errors for regions/seasons abundant of uniform plane-parallel types of clouds, for example, stratus clouds along the cold waters of west coasts and clouds in the winter storm tracks. Figure 10 is similar to Fig. 6 but for fluxes, together with nonlinear curve fits to each of the flux datasets as a function of cloud optical depth. The fluxes were calculated based on solar insolation of 1365 W m^{-2} multiplied by TOA albedos and the cosine of SZA for individual ERBE overcast pixel. The nonlinear curve-fitting functions are

$$F(\tau) = c_0 + c_1[1 - \exp(-c_2\tau)], \qquad (4)$$

where F is the flux and τ the cloud optical depth; and c_0, c_1, and c_2 are fitting coefficients, as shown in Table 2. For a plane-parallel cloud of known optical depth, one may use this equation to approximately estimate the uncertainty in ERBE-inverted flux. The overall means of the two sets of fluxes and the rms biases of the curve fits are also indicated in the figure. The modeled mean fluxes are generally smaller than the ERBE-inverted mean fluxes, except for SZA $\approx$ 76.8°. The mean differences between ERBE-inverted and modeled fluxes are about 4 W m^{-2} for SZA $\approx$ 33.1° and about 8–12 W m^{-2} for larger SZAs. Although the overall mean differences between ERBE and modeled fluxes are with-
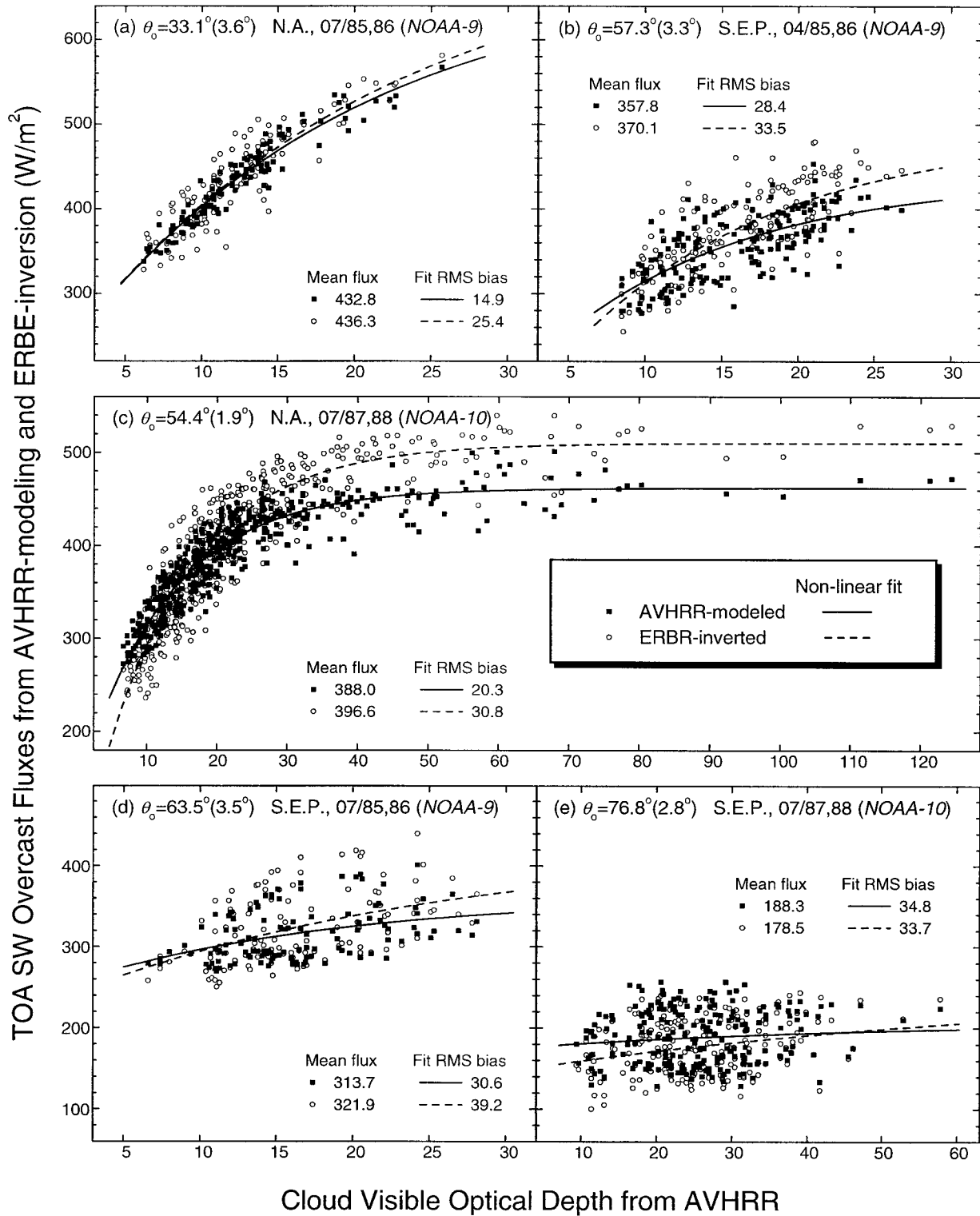
FIG. 10. Comparisons between ERBE-observed and AVHRR-modeled SW TOA overcast fluxes as a function of cloud visible optical depth. Each point is for a $(50 \text{ km})^2$ ERBE pixel. Nonlinear curve fits to each set of fluxes are plotted. The mean fluxes and the rms differences of the fits are indicated in each panel, along with regions, months, satellites, and SZAs of the observations.

TABLE 2. The coefficients c_0, c_1, and c_2 of the curve-fitting function given by Eq. (4) fitted to AVHRR-modeled and ERBE-inverted TOA fluxes.

	AVHRR modeled			ERBE inverted		
	c_0	c_1	c_2	c_0	c_1	c_2
(a)$\theta_0 = 33.1°$	204.644	481.624	0.052 965	207.404	516.781	0.048 079
(b)$\theta_0 = 57.3°$	163.235	273.219	0.081 044	113.727	377.518	0.074 771
(c)$\theta_0 = 54.4°$	132.485	329.324	0.080 204	41.745	468.465	0.076 801
(d)$\theta_0 = 63.5°$	245.840	117.678	0.055 771	228.626	199.219	0.036 845
(e)$\theta_0 = 76.8°$	173.940	32.931	0.022 533	147.158	106.510	0.013 776

in the rms biases of the fits, the mean flux difference varies considerably with cloud optical depth. For large cloud optical depths such as the clouds associated with winter storm tracks or other large-scale storms of uniform cloud tops, the differences can be as large as 40–50 W m^{-2}.

5. Summary and discussions

Coincident and collocated satellite observations from the Earth Radiation Budget Experiment (ERBE) and Advanced Very High Resolution Radiometer (AVHRR) were used to examine the dependence of both shortwave (SW) top-of-atmosphere (TOA) reflectance and albedo on cloud optical properties. The study was restricted to completely overcast scenes covered by low-level, single-layered, marine stratus with uniform cloud tops observed over two oceanic regions. Satellite observations were constrained to viewing zenith angles (VZAs) smaller than 30°. Uniform overcast cloud scenes were identified by applying the spatial coherence method to the AVHRR 11-μm GAC (global area coverage) data. Cloud-top temperatures were limited to higher than 273 K to ensure that the clouds were composed of water droplets only and the standard deviations were less than 1 K to retain only clouds of relatively flat tops. Cloud properties, including optical depth, droplet effective radius, and top emission temperature, were retrieved respectively from AVHRR 0.63-, 3.7-, and 11-μm radiance measurements. They were then employed in an adding–doubling radiative transfer model to compute SW TOA reflectance and albedos (henceforth AVHRR-modeled reflectance/albedo) for comparisons with coincident and collocated ERBE observations. The comparisons helped evaluate both the fundamentals of solar radiative transfer within clouds and the ERBE satellite inversion processes.

Coincident ERBE and AVHRR measurements made from *NOAA-9* and *NOAA-10* satellites have the advantage of small data matching errors. The ERBE instantaneous reflectance measurements were calibrated on board with an accuracy of within 0.6% (Barkstrom et al. 1989). AVHRR radiance measurements were calibrated postlaunch following the method used in the International Satellite Cloud Climatology Project (ISCCP) that has an uncertainty of about 1%–2% (Brest et al. 1997). AVHRR data have been successfully employed

to retrieve cloud properties with a reported uncertainty on the order of 10% (Nakajima and Nakajima 1995; Platnick and Valero 1995).

The selection of uniform overcast scenes covered by low-level, single-layered, marine stratus clouds was aimed to remove the influence of broken clouds. Identification of such cloud scenes was based on the spatial coherence method (Coakley and Bretherton 1982). The method could underestimate cloud cover in case of semitransparent clouds and thin cirrus clouds (Luo et al. 1994). Cloud-top temperatures and their variations were thus both constrained to ensure the uniformity of the selected overcast scenes. To minimize angular biases due to the plane-parallel assumption, the comparisons were limited to near-nadir views (VZA < 30°). Nevertheless, biases may still exist, especially for large solar zenith angles (SZA) (Loeb and Coakley 1998).

The comparisons between ERBE-observed and AVHRR-modeled reflectances showed good agreements in terms of both magnitude and trend of variation for all regions and months under study with different SZAs. The mean differences were less than 0.007 (absolute) or 1.6% (relative), respectively, with an rms difference <0.02 (absolute). These values are smaller or comparable to the magnitudes of the calibration uncertainties for ERBE and AVHRR measurements. Yet the differences showed no apparent dependence on any of the physical parameters examined (cloud optical depth, top height, droplet effective radius, SZA, etc.). Since no inversion algorithm was involved in obtaining the ERBE reflectance data, the good agreements bolster our confidence on the fundamentals of solar radiative transfer in such ideal cloudy conditions.

However, comparisons between ERBE-inverted and AVHRR-modeled albedos showed large discrepancies and strong variations with cloud optical depth and SZA. For small SZA (~33°), the mean differences were small, <0.005 (absolute) or 1% (relative), for all cloud optical depths. For moderate SZA (~60°), the mean differences increased significantly with increasing cloud optical depth, that is, close to zero for cloud optical depths around 10 but larger than 0.05 (absolute) or 10% (relative) for cloud optical depths >25. For large SZA (~76.8°), the mean differences were negative with the largest magnitude close to 0.10 (absolute) or 20% (relative) occurring at small cloud optical depths. Overall, the rms differences were close to the uncertainty of

0.038 claimed for instantaneous ERBE albedo data (Wielicki et al. 1995). Many factors may contribute to the differences such as observation uncertainties due to calibration, scene identification, and angular dependence correction (Suttles et al. 1992; Wielicki et al. 1995), as well as model uncertainties due to plane-parallel assumption. From this study, it appears that the dominant factors are the angular correction and plane-parallel assumption. The latter tends to overestimate cloud optical depths and TOA albedos at large SZAs (Loeb and Davies 1996), which explains at least partially the large systematic differences found in Fig. 6e. The dependence of the differences on cloud optical depths is attributed mainly to the use of a single ERBE angular dependence model (ADM) that was applied to all overcast scenes.

Unlike reflectance that was measured directly, ERBE albedos were converted from reflectances by means of angular correction using a set of ADMs for 12 distinct scene types determined by the ERBE scene identification scheme (Smith et al. 1986; Wielicki and Green 1989). For cloudy scenes, ERBE ADMs were only differentiated according to four cloud amounts, that is, clear, partly cloudy, mostly cloudy, and overcast (Suttles et al. 1988). A single average overcast ADM was applied to all overcast scenes, regardless of the cloud optical or microphysical properties, leading to bias errors in the retrieved albedos/fluxes (Wielicki et al. 1996). Using satellite observations from the ScaRaB radiometer, Chang et al. (2000) investigated the biases resulting from the use of a single ADM for thin, thick, warm, and cold overcast clouds. The errors range from 0.01 to 0.04, depending on the viewing geometry and characteristics of the overcast scenes.

By comparing the ERBE ADMs with those simulated by the model, it appears that the variations of discrepancies with cloud optical depth and SZA can be well explained by differences in the ADMs. In general, the ERBE overcast ADM resembles the model-simulated overcast ADM for a larger cloud optical depth, whereas the ERBE mostly cloudy ADM resembles the modeled one for a smaller cloud optical depth. For example, for SZA $\approx 75°$ (with nadir VZAs $< 30°$), the ERBE overcast ADM resembles the modeled overcast ADM for a cloud optical depth of 128, but the ERBE mostly cloudy ADM resembles the modeled one for a cloud optical depth of 24. For SZA $\approx 60°$, the ERBE overcast ADM resembles the modeled ADM for a cloud optical depth of 40, but the ERBE mostly cloudy ADM resembles the modeled one for a cloud optical depth of 16. For smaller SZAs, the ERBE overcast and mostly cloudy ADMs are similar, and both resemble the modeled ADM for a cloud optical depth of 16.

In addition, the performance and influence of the ERBE scene identification were also examined. With reference to AVHRR-based scene types, nearly all of the uniform low-level, single-layered, marine overcast clouds were classified as mostly cloudy by ERBE. How-ever, such scene misidentification had no adverse impact on the inversion of ERBE reflectance to albedo. In fact, the agreement between ERBE-observed and AVHRR-modeled albedos deteriorates if the ERBE mostly cloudy ADM is replaced by the overcast ADM. The mean differences are even larger with an opposite sign and the rms differences increase as well, but the dependence on cloud optical depth remains. The finding suggests that the same scene identification scheme should be used in the development and application of an ADM, even though the scene type may be identified incorrectly.

To date, most climate studies using radiation budget data have focused on mean fluxes that affect the large-scale thermodynamic state of the climate. The mean differences between ERBE and AVHRR-modeled TOA radiative fluxes are on the order of 4–12 W m^{-2}, similar to the discrepancies found by others between observations and modeling (Rossow and Zhang 1995; Li et al. 1997). However, the strong dependence of the discrepancies on cloud optical depth as revealed here may increase the differences up to 40–50 W m^{-2} for systematically large or small cloud optical depths. Cloud properties, like optical depth, vary on a latitudinal, seasonal, or day-to-day basis, which also link to temperature variations (Tselioudis et al. 1992). Cloud-radiation feedback is the leading cause for the uncertainties in modeling climate and its changes (Intergovernmental Panel on Climate Change 1995; Cess et al. 1990). An improved understanding of the feedback requires nonbiased determination of TOA radiative fluxes, especially with regard to cloud properties. The findings of this study therefore underscore the importance of differentiating cloud properties in the ADMs, as to be developed and used in the Clouds and the Earth Radiant Energy System (Wielicki et al. 1996).

REFERENCES

Ackerman, S. A., and T. Inoue, 1994: Radiation energy budget studies using collocated AVHRR and ERBE observations. *J. Appl. Meteor.,* **33,** 370–378.

Arking, A., 1991: The radiative effects of clouds and their impact on climate. *Bull. Amer. Meteor. Soc.,* **72,** 795–813.

——, and J. D. Childs, 1985: The retrieval of cloud cover parameters from multispectral satellite images. *J. Climate Appl. Meteor.,* **24,** 322–333.

——, M.-D. Chou, and W. L. Ridgway, 1996: On estimating the effects of clouds on atmospheric absorption based on flux observations above and below cloud level. *Geophy. Res. Lett.,* **23,** 829–832.

Baldwin, D. G., and J. A. Coakley Jr., 1991: Consistency of earth radiation budget experiment bidirectional models and the observed anisotropy of reflected sunlight. *J. Geophys. Res.,* **96,** 5195–5207.

Barker, H. W., Z. Li, and J.-P. Blanchet, 1994: Radiative characteristics of the Canadian Climate Centre second-generation general circulation model. *J. Climate.,* **7,** 1070–1091.

Barkstrom, B. R., and G. L. Smith, 1986: The Earth Radiation Budget Experiment: Science and implementation. *Rev. Geophys.,* **24,** 379–390.

——, and Coauthors, 1989: Earth Radiation Budget Experiment (ERBE) archival and April 1985 results. *Bull. Amer. Meteor. Soc.,* **70,** 1254–1262.

Betts, A. K., P. Minnis, W. Ridgway, and D. F. Young, 1992: Integration of satellite and surface data using a radiative-convective oceanic boundary-layer model. *J. Appl. Meteor.,* **31,** 340–350.

Bohren, C. F., and D. R. Huffman, 1983: *Absorption and Scattering of Light by Small Particles.* John Wiley and Sons, 530 pp.

Brest, C. L., W. B. Rossow, and M. D. Roiter, 1997: Update of radiance calibrations for ISCCP. *J. Atmos. Oceanic Technol.,* **14,** 1091–1109.

Cess, R. D., and Coauthors, 1990: Interpretation of climate feedback processes in 19 atmospheric general circulation models. *J. Geophys. Res.,* **95,** 16 601–16 615.

——, G. L. Potter, W. L. Gates, J.-J. Morcrette, and L. Corsetti, 1992: Comparison of general circulation models to Earth Radiation Budget Experiment data: Computation of clear-sky fluxes. *J. Geophys. Res.,* **97,** 20 421–20 426.

——, and Coauthors, 1995: Absorption of solar radiation by clouds: Observations versus models. *Science,* **267,** 496–499.

Chang, F.-L., 1997: Properties of low-level marine clouds as deduced from AVHRR satellite observations. Ph.D. dissertation, Oregon State University, 335 pp.

——, Z. Li, and A. P. Trishchenko, 2000: The dependence of TOA reflectance anisotropy on cloud properties inferred from ScaRaB satellite data. *J. Appl. Meteor.,* in press.

Chou, M.-D., 1992: A solar radiation model for climate studies. *J. Atmos. Sci.,* **49,** 762–772.

Coakley, J. A., Jr., and F. P. Bretherton, 1982: Cloud cover from high-resolution scanner data: Detecting and allowing for partially filled fields of view. *J. Geophys. Res.,* **87,** 4917–4932.

——, and D. G. Baldwin, 1984: Towards the objective analysis of clouds from satellite imagery data. *J. Climate Appl. Meteor.,* **23,** 1065–1099.

Fu, Q., 1996: An accurate parameterization of the solar radiative properties of cirrus clouds for climate models. *J. Climate,* **9,** 2058–2082.

Goody, R. M., and Y. L. Yung, 1989: *Atmospheric Radiation: Theoretical Basis.* Oxford University Press, 519 pp.

Hale, G. M., and M. R. Querry, 1973: Optical constants of water in the 200 nm to 200 mm wavelength region. *Appl. Opt.,* **12,** 555–563.

Han, Q., W. B. Rossow, and A. A. Lacis, 1994: Near-global survey of effective droplet radii in liquid water clouds using ISCCP data. *J. Climate,* **7,** 465–497.

Han, W., K. Stamnes, and D. Lubin, 1999: Remote sensing of surface and cloud properties in the Arctic from AVHRR measurements. *J. Appl. Meteor.,* **38,** 989–1012.

Hansen, J. E., 1971: Multiple scattering of polarized light in planetary atmospheres. Part II: Sunlight reflected by terrestrial water clouds. *J. Atmos. Sci.,* **28,** 1400–1426.

Harrison, E. F., P. Minnis, B. R. Barkstrom, V. Ramanathan, R. D. Cess, and G. G. Gibson, 1990: Seasonal variation of cloud radiative forcing derived from the Earth Radiation Budget Experiment. *J. Geophys. Res.,* **95,** 18 687–18 703.

Hartmann, D. L., V. Ramanathan, A. Berroir, and G. E. Hunt, 1986: Earth Radiation Budget data and climate research. *Rev. Geophys.,* **24,** 439–468.

Hu, Y. X., and K. Stamnes, 1993: An accurate parameterization of the radiative properties of water clouds suitable for use in climate models. *J. Climate,* **6,** 728–742.

Intergovernmental Panel on Climate Change, 1995: *Climate Change, 1994: Radiative Forcing of Climate Change and an Evaluation of the IPCC 1992 Emission Scenarios.* Cambridge University Press, 339 pp.

Kidwell, K. B., 1991: *NOAA Polar Orbiter Data Users Guide.* NOAA National Climate Data Center, Satellite Data Services Division, Washington, D.C., 250 pp. [Available from Department of Commerce, NOAA National Climatic Data Center, Satellite Data Services Division, Washington, DC 20233.]

Kiehl, J. T., and V. Ramanathan, 1990: Comparison of cloud forcing derived from the Earth Radiation Budget Experiment with that simulated by the NCAR Community Climate Model. *J. Geophys. Res.,* **95,** 11 679–11 698.

Kneizys, F. X., E. P. Shettle, L. W. Arbeu, J. H. Chetwynd, G. P. Anderson, W. O. Gallery, J. E. A. Selby, and S. A. Clough, 1988: Users Guide to LOWTRAN-7. Air Force Geophysics Laboratory Tech. Rep. AFGL-TR-88-0177, 137 pp. [Available from Phillips Laboratory, Geophysics Directorate, Hanscom AFB, MA 01731-3010.]

Lau, N.-C., and M. W. Crane, 1995: A satellite view of the synoptic-scale organization of cloud properties in midlatitude and tropical circulation systems. *Mon. Wea. Rev.,* **123,** 1984–2006.

Li, Z., 1996: On the angular correction of satellite radiation measurements: The performance of ERBE angular dependence model in Arctic. *Theor. Appl. Climatol.,* **54,** 235–248.

——, and H. G. Leighton, 1991: Scene identification and its effect on cloud radiative forcing in the Arctic. *J. Geophys. Res.,* **96,** 9175–9188.

——, and A. Trishchenko, 1999: A study toward an improved understanding of the relationship between visible and shortwave measurements. *J. Atmos. Oceanic Technol.,* **16,** 347–360.

——, H. W. Barker, and L. Moreau, 1995: The variable effect of clouds on atmospheric absorption of solar radiation. *Nature,* **376,** 486–490.

——, L. Moreau, and A. Arking, 1997: On solar energy disposition: A perspective from observation and modeling. *Bull. Amer. Meteor. Soc.,* **78,** 53–70.

Loeb, N. G., and R. Davies, 1996: Observational evidence of plane parallel model biases: Apparent dependence of cloud optical depth on solar zenith angle. *J. Geophys. Res.,* **101,** 1621–1634.

——, and J. A. Coakley Jr., 1998: Inference of marine stratus cloud optical depths from satellite measurements: Does 1D theory apply? *J. Climate,* **11,** 215–233.

Luo, G., X. Lin, and J. A. Coakley Jr., 1994: 11-μm emissivities and droplet radii for marine stratocumulus. *J. Geophys. Res.,* **99,** 3685–3698.

McClatchey, R. A., R. W. Fenn, J. E. Selby, F. E. Volz, and J. S. Garing, 1972: Optical properties of the atmosphere. Air Force Cambridge Research Laboratories Rep. AFCRL-72-0497, 108 pp. [Available from Air Force Cambridge Research Laboratories, Hanscom AFB, MA 01731.]

Nakajima, T. Y., and T. Nakajima, 1995: Wide-area determination of cloud microphysical properties from NOAA AVHRR measurements for FIRE and ASTEX regions. *J. Atmos. Sci.,* **52,** 4043–4059.

——, M. D. King, J. D. Spinhirne, and L. F. Radke, 1991: Determination of the optical thickness and effective particle radius of clouds from reflected solar radiation measurements. Part II: Marine stratocumulus observations. *J. Atmos. Sci.,* **48,** 728–750.

Payne, R. E., 1972: Albedo of the sea surface. *J. Atmos. Sci.,* **29,** 959–970.

Pilewskie, P., and F. P. J. Valero, 1995: Direct observations of excess solar absorption by clouds. *Science,* **257,** 1626–1629.

Platnick, S., and S. Twomey, 1994: Determining the susceptibility of cloud albedo to changes in droplet concentration with the Advanced Very High Resolution Radiometer. *J. Appl. Meteor.,* **33,** 334–347.

——, and E. P. J. Valero, 1995: A validation study of a satellite cloud retrieval during ASTEX. *J. Atmos. Sci.,* **52,** 2985–3001.

Ramanathan, V., R. D. Cess, E. F. Harrison, P. Minnis, B. R. Barkstrom, E. Ahmad, and D. L. Hartmann, 1989: Cloud radiative

forcing and climate: Results from the Earth Radiation Budget Experiment. *Science,* **243,** 57–63.

——, B. Subasilar, G. J. Zhang, W. Conant, R. D. Cess, J. T. Kiehl, H. Grassl, and L. Shi, 1995: Warm pool heat budget and shortwave cloud forcing: A missing physics? *Science,* **267,** 499–503.

Rodgers, R. R., and M. K. Yau, 1989: *A Short Course in Cloud Physics.* 3d ed. Pergamon Press, 293 pp.

Rossow, W. B., and R. A. Schiffer, 1991: ISCCP cloud data products. *Bull. Amer. Meteor. Soc.,* **71,** 2–20.

——, and Y.-C. Zhang, 1995: Calculation of surface and top of atmosphere radiative fluxes from physical quantities based on ISCCP data sets. 2. Validation and first results. *J. Geophys. Res.,* **100,** 1167–1197.

Slingo, A., 1989: A GCM parameterization for the shortwave radiative properties of water clouds. *J. Atmos. Sci.,* **46,** 1419–1427.

Smith, G. L., R. N. Green, E. Raschke, L. M. Avis, J. T. Suttles, B. A. Wielicki, and R. Davies, 1986: Inversion methods for satellite studies of the earth's radiation budget: Development algorithms for the ERBE mission. *Rev. Geophys.,* **24,** 407–421.

Stephens, G. L., 1978: Radiation profiles in extended water clouds. Part II: Parameterization schemes. *J. Atmos. Sci.,* **35,** 2123–2132.

——, and C. M. R. Platt, 1987: Aircraft observations of the radiative and microphysical properties of stratocumulus and cumulus cloud fields. *J. Climate Appl. Meteor.,* **26,** 1243–1269.

——, G. G. Campbell, and T. H. Vonder Harr, 1981: Earth radiation budgets. *J. Geophys. Res.,* **86,** 9739–9760.

Stuhlmann, R., and E. Raschke, 1987: Satellite measurements of the earth radiation budget: Sampling and retrieval of short wave exitances—a sampling study. *Beitr. Phys. Atmos.,* **60,** 393–410.

Suttles, J. T., and Coauthors, 1988: Angular radiation models for Earth–atmosphere system. Vol. I—Shortwave radiation. NASA RP-1184, 144 pp. [Available from NASA, Scientific and Technical Information Division, Washington, DC 20546-0001.]

——, B. A. Wielicki, and S. Vemury, 1992: Top-of-atmosphere radiative fluxes: Validation of ERBE scanner inversion algorithm using *Nimbus-7* ERB data. *J. Appl. Meteor.,* **31,** 784–796.

Thekaekara, M. P., 1974: Extraterrestrial solar spectrum, 3000-6100Å at 1-Å intervals. *Appl. Opt.,* **13,** 518–522.

Tselioudis, G., W. B. Rossow, and D. Rind, 1992: Global patterns of cloud optical thickness variation with temperature. *J. Climate,* **5,** 1484–1495.

Wielicki, B. A., and R. N. Green, 1989: Cloud identification for ERBE radiative flux retrieval. *J. Appl. Meteorol.,* **28,** 1133–1146.

——, R. D. Cess, M. D. King, D. A. Randall, and E. F. Harrison, 1995: Mission to Planet Earth: Role of clouds and radiation in climate. *Bull. Amer. Meteor. Soc.,* **76,** 2125–2153.

——, B. R. Barkstrom, E. F. Harrison, R. B. Lee III, G. L. Smith, and J. E. Cooper, 1996: Cloud and the Earth Radiant Energy System (CERES): An Earth Observing System experiment. *Bull. Amer. Meteor., Soc.,* **77,** 853–868.

Ye, Q., and J. A. Coakley Jr., 1996: Biases in earth radiation budget observations, Part II: Consistent scene identification and anisotropic factors. *J. Geophys. Res.,* **101,** 21 253–21 263.